



Direct numerical simulation of pore-scale flow in a bead pack: Comparison with magnetic resonance imaging observations



Xiaofan Yang^a, Timothy D. Scheibe^{a,*}, Marshall C. Richmond^a, William A. Perkins^a, Sarah J. Vogt^b, Sarah L. Codd^c, Joseph D. Seymour^b, Matthew I. McKinley^a

^a Pacific Northwest National Laboratory, Hydrology Group, PO Box 999, MS K9-36, Richland, WA 99352, United States

^b Montana State University, Dept. Of Chemical and Biological Engineering, 306 Cobleigh Hall, Bozeman, MT 59717, United States

^c Montana State University, Dept. Of Mechanical and Industrial Engineering, 201F Roberts Hall, Bozeman, MT 59717, United States

ARTICLE INFO

Article history:

Received 28 August 2012

Received in revised form 31 January 2013

Accepted 31 January 2013

Available online 27 February 2013

Keywords:

Pore-scale modeling

Porous media flow

Magnetic resonance imaging

Validation

Computational fluid dynamics

ABSTRACT

A significant body of current research is aimed at developing methods for numerical simulation of flow and transport in porous media that explicitly resolve complex pore and solid geometries, and at utilizing such models to study the relationships between fundamental pore-scale processes and macroscopic manifestations at larger (i.e., Darcy) scales. A number of different numerical methods for pore-scale simulation have been developed, and have been extensively tested and validated for simplified geometries. However, validation of pore-scale simulations of fluid velocity for complex, three-dimensional (3D) pore geometries that are representative of natural porous media is challenging due to our limited ability to measure pore-scale velocity in such systems. Recent advances in magnetic resonance imaging (MRI) offer the opportunity to measure not only the pore geometry, but also local fluid velocities under steady-state flow conditions in 3D and with high spatial resolution. In this paper, we present a 3D velocity field measured at sub-pore resolution (tens of micrometers) over a centimeter-scale 3D domain using MRI methods. We have utilized the measured pore geometry to perform 3D simulations of Navier–Stokes flow over the same domain using direct numerical simulation techniques. We present a comparison of the numerical simulation results with the measured velocity field. It is shown that the numerical results match the observed velocity patterns well overall except for a variance and small systematic scaling which can be attributed to the known experimental uncertainty in the MRI measurements. The comparisons presented here provide strong validation of the pore-scale simulation methods and new insights for interpretation of uncertainty in MRI measurements of pore-scale velocity. This study also provides a potential benchmark for future comparison of other pore-scale simulation methods. © 2012 Elsevier Science. All rights reserved.

© 2013 Published by Elsevier Ltd.

1. Introduction

Conventional simulations of porous media flow and solute transport, commonly applied at physical scales ranging from laboratory columns up to field-scale aquifers, utilize a spatially averaged conceptualization that neglects the details of pore and solid geometry. Instead, rates and directions of flow and solute transport are defined over a “representative elementary volume” (REV) of porous media for which the effects of variations in fluid velocity and solute diffusion within individual pores are approximated by apparent or upscaled model forms and parameters (e.g., Darcy’s law and the advection–dispersion equation, parameterized by the hydraulic conductivity tensor and longitudinal and transverse dispersivities). Recently, there has been increased interest in

problems that manifest anomalous (non-Fickian) dispersion at macroscopic scales, e.g. [1,2], problems that are characterized by sharp local gradients and mixing-controlled reactions, e.g. [3–8], and problems that involve moving interfaces at the pore scale, e.g., [9–14]. A number of recent studies have explored these issues using pore-scale simulators, in which the geometry of pore spaces and solid materials is explicitly considered and processes are defined at the sub-pore (e.g., micrometer to millimeter) scale. As pointed out by [15], pore-scale simulators have significant utility in that they provide a mechanism for defining (and potentially parameterizing) macroscopic processes in a manner that properly accounts for the character of fundamental pore-scale processes and the pore-scale structure of porous media. Advances in three-dimensional (3D) characterization of porous media structure, using methods such as X-ray computed tomography (XCT) and magnetic resonance imaging (MRI), have provided new tools for quantifying pore geometry with sufficient resolution to facilitate pore-scale

* Corresponding author. Tel.: +1 509 372 6065; fax: +1 509 372 6089.

E-mail address: Tim.Scheibe@pnnl.gov (T.D. Scheibe).

simulations. Simultaneous advances in high-performance computing have provided the computational power necessary to perform pore-scale simulations over complex 3D domains. However, the validation of pore-scale simulations in complex 3D geometries remains a significant challenge, because of the difficulty of observing processes occurring within internal pore spaces under flowing conditions without disturbing the flow pattern.

In this paper, we present a method for validation of pore-scale single-phase steady flow simulations based on measurement of pore-scale velocities in 3D using MRI. We have performed both numerical simulation and measurement of 3D velocity fields in a centimeter-scale column filled with uniform polystyrene beads. CFD simulations are performed in the laminar regime and a general evaluation of simulation results is performed based on overall mass balances, predicted pressure drop, and other macroscopic measures. Finally, we compare the simulated velocity field directly with the experimental observations at the microscale in order to (1) provide a general test/validation of the pore-scale simulation approach; (2) evaluate potential impacts of two alternative approaches to meshing of pore-scale geometry; and (3) identify discrepancies between simulated and observed velocity fields and their potential causes.

2. Methods

2.1. Pore-scale flow simulation approaches

Traditional numerical simulations of porous media flow utilize a conceptualization of the porous medium that neglects the geometric details of discrete individual solid grains and intervening pore spaces, and instead treats the porous medium as an effective continuum. Here we refer to this conceptualization as the “Darcy scale,” reflecting the well-known Darcy’s Law that describes flow averaged over some representative volume containing many solid grains and pore bodies, typically at least millimeter to centimeter scales. Alternatively, in recent decades it has become possible to explicitly simulate processes at the pore scale, at which the details of solid and pore geometry can be directly incorporated and velocity variations can be resolved at the scale of tens of micrometers or smaller. Since many porous media processes of current interest such as biogeochemical reactions or, diffusion-limited mass transfer are strongly impacted by processes occurring at the pore scale, these models have proven useful for gaining new insights into the relationship between fundamental processes defined at the pore scale and upscaled phenomena observed at Darcy scales.

Several alternative approaches to pore-scale modeling have been developed and applied, and are briefly discussed here. The most commonly-used methodology is the Lattice-Boltzmann (LB) method (e.g., [16–25]), which is a discrete method which moves and collides fluid particles on a fixed lattice according to specified rules that are designed such that the time-averaged particle motions are consistent with the Navier–Stokes equations [26,27]. The Smoothed Particle Hydrodynamics (SPH) method, developed originally for simulation of astrophysical flows, has recently been applied to a number of porous media flow and reactive transport problems [4,7,9,28–32]. SPH is a fully lagrangian mesh-free particle-based method, and is therefore particularly robust for application to problems involving moving interfaces in which the system geometry is dynamic (such as multiphase flow or precipitation/dissolution reactions). In contrast to the LB method, SPH directly solves discretized forms of the partial differential equations describing fluid flow and other porous media dynamics. The computational fluid dynamics approach (CFD, alternatively referred to as direct numerical simulation or DNS) is similar to SPH in that it solves discretized forms of the governing partial differential

equations, but differs from SPH in that it does so on a designated mesh (e.g., finite volume, finite element, or finite difference). CFD methods have been widely applied to a number of fluid flow problems and are routinely used in design of aircraft, automobiles, turbines, and other engineered systems. Their application to pore-scale flow modeling is conceptually straightforward but requires development of complex meshes to represent irregular pore geometries. The CFD approach is computationally more efficient than SPH for large single-phase steady flow problems, such as the problem considered in this work, but its implementation for the simulation of problems with moving interfaces is more complex. Applications of CFD methods to simulate pore-scale porous media flow and transport processes include [8,33–39]. The fourth major pore-scale modeling approach is the pore-network modeling method, which approximates the pore geometry by a set of interconnected pore throats (e.g., tube-like structures) and pore bodies (e.g., sphere-like structures). This method retains the complete topology of a measured pore geometry, but does not represent the actual details of the pore geometry in the manner of the other methods. Because the solution of partial differential equations for the pore network model reduces to simultaneous solution of a set of analytical solutions for flow in each network element, the pore network method is less computationally demanding than the other approaches, and has been successfully applied to a broad range of problem types (e.g., [11–13,40–48]). While each of these four methodologies has been successfully applied to simulate pore-scale fluid flow and other processes, there has not yet been a systematic comparison of these different methodologies for a complex problem representative of real porous media.

2.2. Measurement of pore-scale velocities using magnetic resonance velocimetry

A critical question for all of the pore-scale modeling methods described above is to what degree they are able to accurately simulate processes in real porous media systems. A number of simple verification tests can be and have been applied to each method, comparing simulation results to simple cases for which known solutions exist. Some processes have also been validated for complex geometric systems, such as the distribution of multiple fluid phases computed at the pore scale and measured using X-ray microtomography [20,49]. However, the validation of computed flow velocities against measurements in arbitrary pore geometries has been limited thus far by our lack of ability to measure pore-scale velocities in a non-invasive manner that does not disturb the flow field. The pore-scale velocity distribution controls many macroscopic phenomena including longitudinal and transverse dispersion, mixing-dependent effective reaction rates, effective porosity and permeability, and is therefore the foundational element of most pore-scale simulations. The focus of this paper is on testing the simulated spatial distributions of pore-scale velocities against experimentally measured values.

Here we address this need by application of magnetic resonance velocimetry (MRV), based on magnetic resonance imaging (MRI) technology, to experimentally measure single-phase fluid velocities in a packed column under steady flow conditions. The MRI method also provides highly-resolved measurement of the solid/pore geometry, and because the experimental conditions are well controlled it is possible to specify a numerical model system that corresponds directly to the experimental system. In this manner we can directly compare measured and simulated pore-scale fluid velocities in a real porous media system, thereby providing a validation test for the pore-scale simulator.

MRI measurement of porous media flow and dispersion have found broad application due to the non-invasive nature of the method [50]. Non spatially resolved MR measurements of

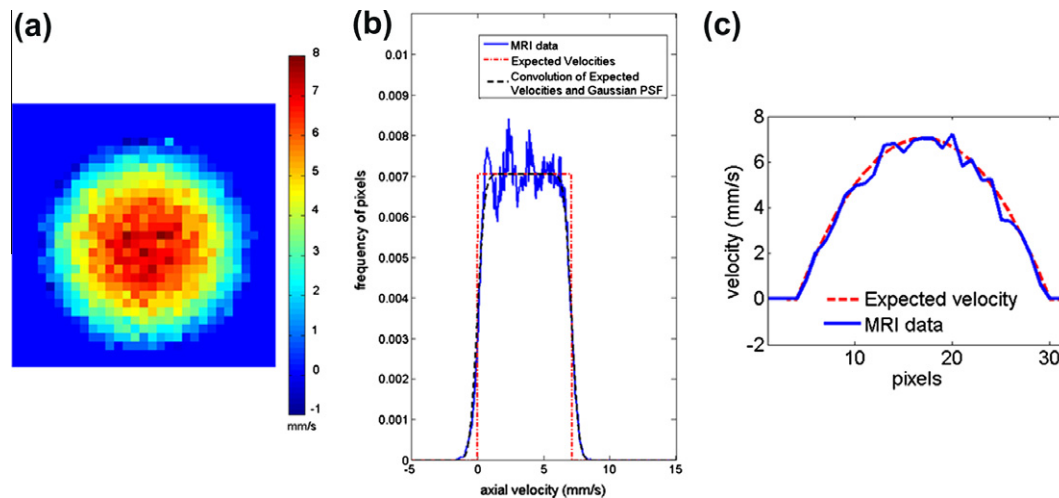


Fig. 1. (a) The MRV image shows a slice from the middle of a 3D velocity data set for water flowing in a 1 mm capillary. (b) The graph shows the histogram of the distribution of velocities. The expected velocities for this system are shown in red, the experimental velocity distribution is shown in blue and the expected velocities convolved with a Gaussian point spread function (PSF) with a variance $\sigma^2 = 0.19 \text{ mm}^2/\text{s}^2 = (0.44 \text{ mm/s})^2$ is shown in black. (c) Velocity profile for a slice through the middle of the capillary, with the calculated Poiseuille profile. (For interpretation of the references to colour in this figure legend, the reader is referred to the web version of this article.)

dispersion demonstrate excellent agreement with reported literature values from a range of experimental methods and with LB simulations [23,24,51,52]. Spatially resolved MRI methods have been used to characterize a range of porous media flows and a feature of the method is a trade-off between spatial resolution and image acquisition time. High spatial resolution of the order of the pore space [24,51–54] requires longer acquisition times, on the order of 10's of minutes to hours, to signal average the reduced number of MR active nuclei (typically ^1H) in a voxel of the image, while coarse grained in space images suitable for multiphase flows with intermittency can be acquired using rapid imaging methods in times of the order of 50 ms [55,56]. These methods have since been applied extensively to characterize the growth of biofilms in porous media and impacts on porous media flow and transport (e.g., [57–61]), and other investigators have used similar methods to characterize flow in various types of porous media (e.g., [62]). Recent reviews of magnetic resonance velocimetry are provided by [50,63]. Recent work has successfully compared CFD flow simulations with MRV observations in the context of medical applications involving flow in human tissues, e.g., [64,65]. Published comparisons of pore-scale simulations of porous media flow with MRI measurements of pore-scale velocities have primarily used LB simulations and the pore scale velocity resolution has been somewhat limited [52,66]. [48] presented a comparison of CFD and MRI velocities based on the experimental work of [67], but that work addressed only a single unit cell with a small number of spheres in a specified packing arrangement (e.g., simple cubic, rhombohedral), repeated periodically in space. [68] compared LB results with MRI measurements, but only in terms of effective dispersion coefficients without direct point-to-point velocity comparisons. To our knowledge the research reported here uses the highest isotropic spatial resolution MRI data of pore scale velocity acquired to date, for direct comparison to pore scale CFD numerical simulations.

2.2.1. Methodology – geometry and velocity measurements

The bead pack used for MRI measurements was constructed of a 10 mm outer diameter, 8.76 mm inner diameter glass NMR tube with home-built polyether ether ketone (PEEK) fittings and polytetrafluoroethylene (PTFE) tubing (GE Scientific). The tube was filled with 500 μm O.D. monodispersed polystyrene beads (Duke

Scientific, Inc.). For the MRV experiments, a high pressure liquid chromatography (HPLC) pump (Pharmacia) was used to flow distilled water at 100 mL/hr through the bead pack. A solution of gadolinium ions (Magnevist) was added to the water to accelerate the magnetic relaxation time to allow faster sequence repetition and hence reduce experimental time.

MRI data was acquired on a 300 MHz magnet networked to a Bruker AVANCE III spectrometer and a Micro2.5 imaging probe with gradients of 1.482 Tesla/meter (T/m) in all three spatial directions. 3D MRI images used for the porous media grid validation were obtained using a standard spin-echo imaging pulse sequence which was optimized to minimize the experimental echo time to maximize the diffusion limited resolution. Non-flowing high resolution images with a field of view (FOV) of 20 mm \times 10 mm \times 10 mm and 1024 \times 512 \times 512 pixels, resulting in an isotropic voxel size of 19.53 μm \times 19.53 μm \times 19.53 μm were obtained over the course of 72 h. 3D MRV experiments with a FOV of 20 mm \times 10 mm \times 10 mm and 512 \times 256 \times 256 pixels, resulting in a voxel size of 39.06 μm \times 39.06 μm \times 39.06 μm were obtained with encoding for velocity in all three directions. A 3.75 ms echo time was used to accommodate the observation time for velocity $\Delta = 2$ ms with gradient duration of $\delta = 1$ ms. In order to obtain two different gradient encoded images from which to evaluate the phase difference proportional to velocity, a positive and negative $g = \pm 0.1482$ T/m were applied, requiring 36 h for acquisition. A gradient phase roll in the direction of fluid flow was accounted for by applying a straight line correction to every voxel within each slice and enforcing the independently measured mass flux of 100 ml/hr. The MRI experimental method was validated by performing initial experiments on a circular capillary with laminar flow, see Fig. 1.

2.2.2. Determination of experimental noise limited velocity resolution

The inherent signal to noise ratio of the voltage signal acquired in a MRV experiment determines the velocity resolution. To determine the velocity resolution of the MRV measurements, MRV data was acquired on a fluid dynamic flow of known velocity spatial distribution, specifically flow in a capillary tube for which the known velocity distribution is:

$$v_z(r) = \frac{2Q}{\pi R^2} \left(1 - \frac{r^2}{R^2} \right)$$

Experimental parameters for the capillary flow experiment resulted in the same voxel resolution and comparable signal to noise ratio as the data for the bead pack. MRV measurement of the spatial distribution of velocities at the same $39.06 \mu\text{m} \times 39.06 \mu\text{m} \times 39.06 \mu\text{m}$ resolution as that of the porous media data provided the expected velocity histogram for parabolic flow, and the average velocity $\langle v \rangle$ was verified by independent measurement of volumetric flow rate $Q = \langle v \rangle \pi R^2$. The velocity uncertainty was thus determined directly from the capillary data and subsequently applied to evaluation of the bead pack data.

Velocities were measured for water flowing in a 1 mm capillary at an average velocity of 3.54 mm/s. The velocity data from one slice in the 3D data set is shown in Fig. 1a), and the velocity histogram from data taken from the entire 3D data set is shown in Fig. 1b). In this simple system of Poiseuille flow in a circular capillary the expected histogram distribution of velocities is an equal amount of every velocity between 0 mm/s and $v_{max} = 7.04 \text{ mm/s}$, see the red line in Fig. 1b). The experimental velocity histogram data is shown in blue in Fig. 1b) and is fit closely when the expected velocities are convolved with a Gaussian point spread function (GPSF) with a variance $\sigma^2 = 0.19 \text{ mm}^2/\text{s}^2 = (0.44 \text{ mm/s})^2$, shown in black in Fig. 1b). This GPSF is expected to be the same for the velocity measurements in the bead pack and corresponds to an uncertainty in the velocity measurements of $\pm 0.44 \text{ mm/s}$.

2.3. Pore-scale flow simulation using CFD

2.3.1. Numerical methods

In this work, the commercial CFD tool STAR-CCM+ (© CD-adapco) and the in-house CFD code TETHYS (Transient Energy Transport Hydrodynamics Simulator), developed at Pacific Northwest National Laboratory, were both used for flow simulations. Both codes can be run on parallel high performance computing clusters. We have applied two independent codes as a means of providing three levels of verification and validation: (1) code verification against standard benchmark problems, (2) cross-code verification on a complex pore-scale simulation, and (3) validation of a complex pore-scale simulation against experimental data. This section introduces the numerical methods used to solve the flow and transport equations in the STAR-CCM+ and TETHYS codes.

STAR-CCM+ was used to simulate pore-scale flow using an unstructured computational mesh fitted to smooth sphere surfaces. This code is well-suited to this application because it has advanced mesh-generation capabilities. TETHYS was used to simulate pore-scale flow using a cubic mesh directly derived from the voxel images of the pore geometry provided by MRI measurements. Comparisons between the outputs of the two codes focuses primarily on evaluation of the effects of the different mesh representations of the pore geometry, but also provides cross-code verification to the degree that similar results are obtained.

Both codes are applied here to obtain a steady-state solution to the well-known three-dimensional Navier–Stokes equations describing incompressible fluid flow at the pore scale. The standard conservation equations of mass and momentum for an incompressible fluid with constant dynamic viscosity are:

$$\text{Mass Conservation equation : } \nabla \cdot \mathbf{v} = 0$$

$$\text{Momentum Conservation equation : } \rho \partial v / \partial t + \rho \mathbf{v} \cdot \nabla v \\ = -\nabla p + \mu \nabla^2 v$$

in which \mathbf{v} is the local velocity vector, t is time, p is pressure, and μ is the dynamic viscosity. In this work, this transient form is solved with fixed boundary conditions over time until a steady solution is achieved, since solution of the transient form is typically more stable numerically.

In both codes, these equations are discretized using standard finite-volume method techniques [69] (slightly different for each code) to obtain a system of algebraic equations that are then solved using advanced linear algebra methods. The commercial CFD simulation software STAR-CCM+ uses a 2nd-order upwind scheme to discretize the convection and diffusion terms in the momentum equations. An implicit 1st-order scheme is adapted for time marching. In TETHYS, the momentum equations are solved using a 2nd-order central differencing scheme on an orthogonal mesh with a three time level scheme to discretize the unsteady term. In both codes, the iterative SIMPLE algorithm [70] is used to couple the velocity and pressure fields. In the predictor step the estimated pressure field is used to solve the momentum equation, resulting in an intermediate velocity field. This velocity field will in general not satisfy the continuity (mass conservation) equation. In the next step of the algorithm, a pressure correction equation is solved. Then the pressure field is updated followed by the correction of the velocity field. This process is repeated until the solution is converged. We used a convergence criterion on the sum of absolute residuals of the local continuity equation as defined by [70] of 10^{-6} , which is set to be at least three to four orders of magnitude smaller than the total system flux.

2.3.2. Preliminary validation tests

Three fundamental laminar flow problems were selected for preliminary validation: channel flow, pipe flow and a lid-driven cavity [71]. Results from both STAR-CCM+ and TETHYS were compared with benchmark and analytical solutions. Both codes achieved very good agreement with the respective analytical or benchmark results for the friction factor and velocity profile in each case.

To test the ability of the codes to solve a pore-scale flow problem, a simple cubic packing structure was used as an additional validation case. This case also provides useful information about the typical mesh resolution that is required to accurately simulate flow in a random bead pack. The structure of a unit cell within a simple cubic (SC) packing structure is shown in Fig. 2a). The length of the cubic cell is 0.5 mm, and the porosity can be varied by modifying the distance between the grain and the boundary of the unit cell. Note that in this configuration, the grains do not actually touch one another unless the grain surface is extended to the unit cell boundary. This model system, while not physically realistic in that aspect, allows comparison of simulation results under variable porosities while retaining the SC packing structure. For the STAR-CCM+ validation tests, a target porosity (θ) of 0.44 close to that of the experimental packed bed was used, while a target value of 0.52 was selected for the TETHYS simulations (corresponding to a different model system). However, the effective porosities of the meshed system differ from the target porosity depending on the mesh resolution used, as summarized in Table 1. A constant differential pressure was applied between the two ends of the packing in the x -direction. Fig. 2b) shows the results of the calculated non-dimensional drag using different unstructured mesh resolutions (different numbers of polyhedral cells, Mesh S1–S7) in STAR-CCM+ simulations. A minimum of five cells in the narrow throat regions was sufficient to produce good results. Similarly, Fig. 2b) displays the results of the non-dimensional drag by using different voxel (Cartesian) mesh resolutions in TETHYS simulations (10–100 cells per diameter, Mesh T1–T7) and different polyhedral mesh resolutions in STAR-CCM+ simulations. Good agreement with literature values of drag and friction factors [61–63] was obtained using both codes. Based on these results, it can be concluded that 15–20 cells per sphere diameter are adequate for current simulations using structured grids, which is similar to the resolution suggested by [72] for a Lattice-Boltzmann simulation.

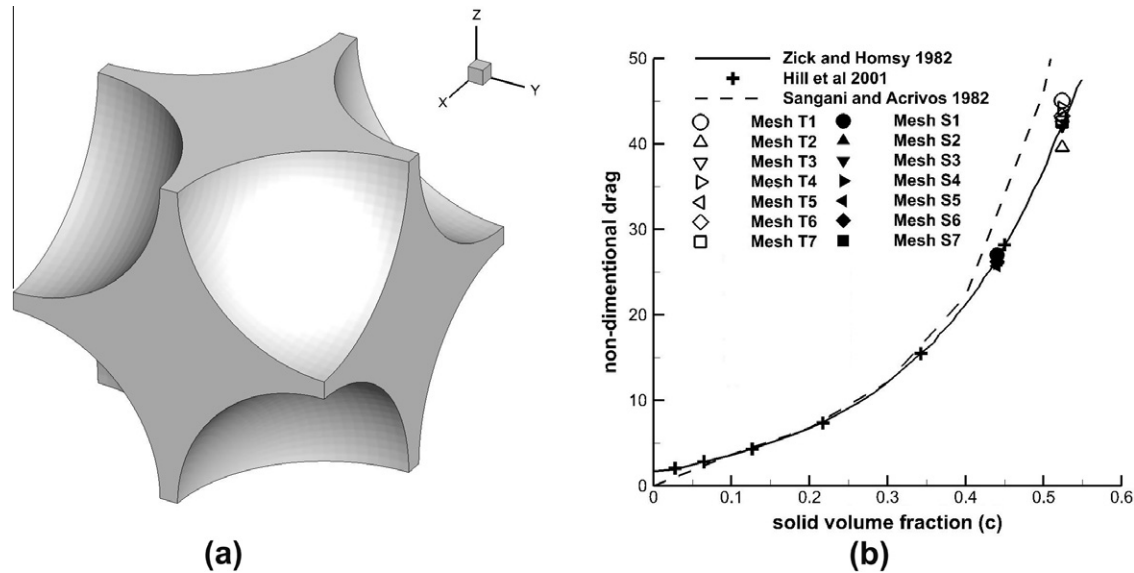


Fig. 2. Simple packing problem as validation cases for both STAR-CCM+ and TETHYS codes: (a) SC packing structure; (b) results of non-dimensional drag using STAR-CCM+ and TETHYS compared to data of [73–75].

Table 1

SC packing: effective porosity estimation for different mesh resolutions in STAR-CCM+ and TETHYS simulations.

$\theta_1 = 0.44$ (STAR-CCM+)	Total number of cells	Cells/throat	Err% of θ_1	$\theta_2 = 0.52$ (TETHYS)	Number of cells per diameter	Cells/throat	Err% of θ_2
Mesh S1	91	0.5	19.181	Mesh T1	10	2	15.713
Mesh S2	355	1	5.483	Mesh T2	15	1	2.648
Mesh S3	1329	2	1.933	Mesh T3	20	2	2.232
Mesh S4	2784	3	1.227	Mesh T4	30	2	0.235
Mesh S5	134646	5	0.202	Mesh T5	40	2	1.460
Mesh S6	561714	7	0.175	Mesh T6	50	2	0.542
Mesh S7	2864596	8	0.164	Mesh T7	100	2	0.113

2.3.3. MRI pore geometry specification

For the TETHYS simulations, the pore geometry was specified directly from the voxel data provided in the MRI geometry dataset, with only a simple threshold algorithm applied to convert voxel intensities into binary (solid/pore) images. Both 20- and 40-micron resolution voxel images were utilized; TETHYS mesh elements corresponded directly to the cubic voxels in the experimental dataset.

In the case of the smoothed-surface boundary-fitted mesh (STAR-CCM+ simulations), more extensive processing of the MRI geometry data was required. The first step was to identify the centroids of all polystyrene beads from the voxel data. For this purpose, we developed and applied an algorithm called “Sphere Loci extraction through Iterative Erosion” or SLIE. The inputs to the SLIE procedure are a block of voxel intensities and a known sphere radius R . The voxel intensities vary over the range [0,1] with values close to 1 representing solid grains. We first make the block binary, classifying voxels as solid or void by comparing the intensities to a threshold, H . In the interest of minimizing subjectivity, H was selected to be 0.5. The assumed value for H may be ill-suited for some data sets and can be determined more accurately by analyzing a histogram of the original data, or by some other objective means. For this dataset, with solids of uniform density, the midpoint threshold is appropriate. The binary data was then eroded by an approximately spherical structured element S with a radius 2 voxels smaller than the known sphere radius R . The erosion operation was carried out using the *imerode* function in the commercial software package MATLAB (© 1994–2012, The MathWorks, Inc). The objective of the erosion process is to shrink the spheres so that they no longer contact one another in the image. After erosion,

connected components are identified using a 26-neighborhood (26-connected voxels are neighbors to every voxel that touches one of their faces, edges, or corners) and their center of masses and volumes are calculated. For each connected component, if the volume is smaller than that of S , that connected component is considered the remnant of a located sphere and its center of mass is recorded as a sphere center. Those connected components whose volume was larger than S are eroded iteratively by a smaller spherical structured element S_i (radii = 3) and subjected in turn to a smaller cutoff volume equal to that of S_i . The process is considered complete when either of the following two conditions are met: (1) there are no sphere centers added at the end of an iteration or (2) no solid voxels remain. The two cutoff volumes were selected to minimize false negative detections. The output of the SLIE algorithm is a listing of the centroid positions and diameters of all beads identified in the MRI geometry image.

For the geometry compilation, the SLIE results were imported into a computer-aided design (CAD) tool implemented in STAR-CCM+. A bounding cylinder with the radius and height of the bead pack was generated in the CAD tool, with extrusions of inlet and outlet added to allow flow development prior to entry into the bead pack. In order to re-construct the bead packing exactly following the images and avoid any sphere loss, the following procedure was executed to automatically generate spheres in STAR-CCM+: (1) sphere centroids were sorted by axial location; (2) the entire bead pack was subdivided into several subsections; (3) spheres were generated for each subsection; (4) solid geometry (spheres) were subtracted from the cylindrical bounding volume to generate pore geometry; (5) each subsection geometric

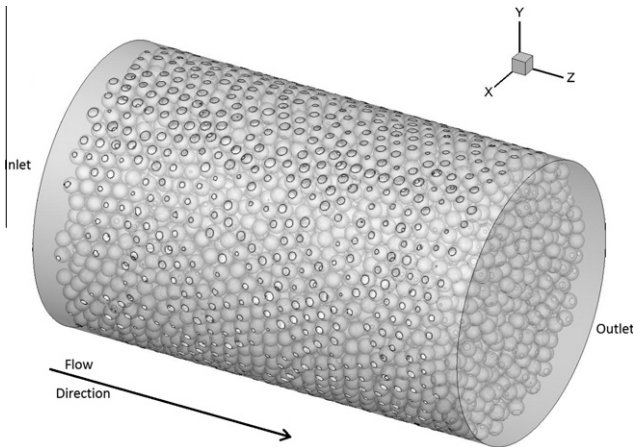


Fig. 3. Visualization of the CAD geometry generated from the application of sphere identification and geometric compilation algorithms to the MRI geometry dataset.

description was exported from STAR-CCM+; and (6) all subsections were imported into the CAD tool and combined together. In all, 6864 spheres were generated by this procedure employing a set of custom Java macros and Matlab programs. A 3D visualization of the generated geometry is shown in Fig. 3, including the flow direction and the locations of the inlet and outlet extensions. Fig. 4 provides a visual comparison between a two-dimensional slice through the generated geometry and the same slice through the MRI-measured geometry, and demonstrates that the geometry compilation process accurately preserves the solid geometry.

2.3.4. Mesh generation

Computational meshes used to represent the solid-pore geometry for the CFD simulations were generated in two ways: (1) direct voxel meshing from the MRI images, and (2) as unstructured space-filling smoothed-surface meshes based on the sphere geometry defined as described above.

The direct voxel meshing approach simply uses cubic mesh elements defined in direct correspondence to the cubic voxel

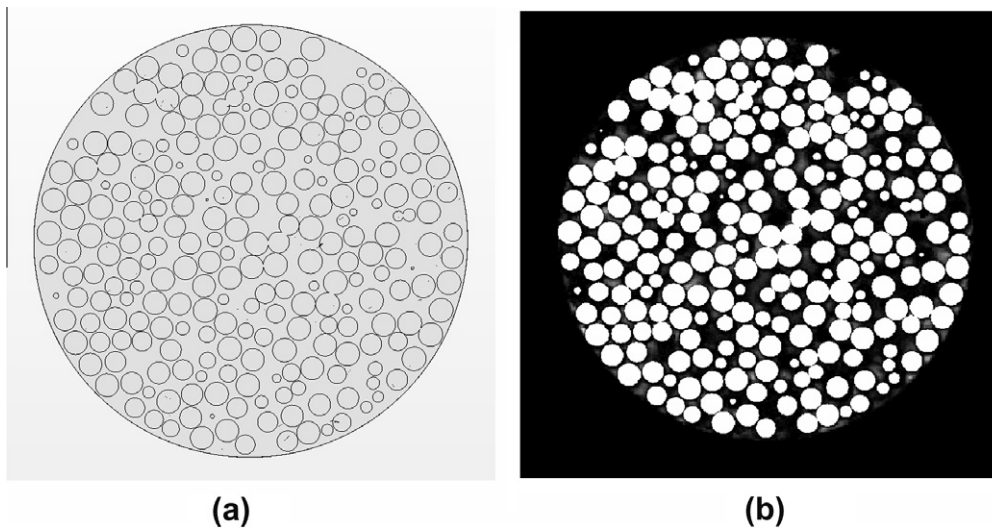


Fig. 4. Visual comparison between (a) the simulation geometry and (b) the experimentally measured geometry for a selected slice from the 3D MRI dataset.

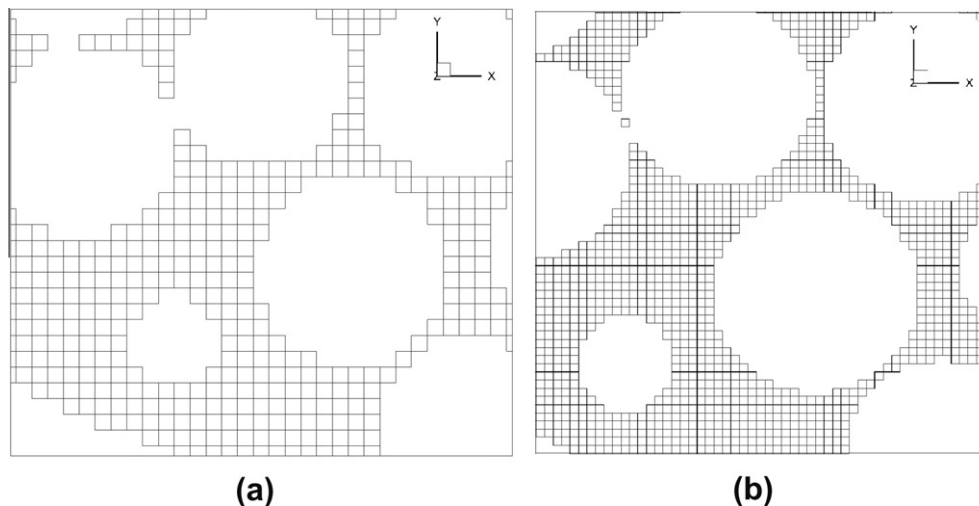


Fig. 5. A portion of slice #320 of (a) the 40-micron voxel mesh and (b) 20-micron voxel mesh showing the stair-step surface effect of directly using the 20- and 40-micron experimental geometries.

elements output from the MRI geometry measurement. The MRI geometries were defined using two different resolutions: 20 and 40 microns. These same mesh resolutions were used directly in the TETHYS CFD simulations for these cases. Note that the cubic voxel meshes approximate the smooth surfaces of the spherical beads in a stair-step manner (as shown in Fig. 5), and therefore potentially introduce some artifacts into the flow simulation caused by artificial surface roughness and differences between the simulated and actual porosity of the packing.

The unstructured smoothed-surface meshes were generated based on the CAD geometry of the spheres described above. These geometric objects were imported into a standard mesh generation package available in STAR-CCM+ for this purpose. A crucial aspect of the mesh generation process is maintaining mesh element quality near particle–particle and particle–wall contact points. These volume elements tend to be highly skewed (which could lead to convergence problems during the calculation) unless the mesh is extremely refined in these areas, which increases the number of cells and as a direct consequence the computational time. Parameters used by the meshing algorithm were controlled to provide adequate mesh refinement in these critical areas (see Table 2). The STAR-CCM+ code was used to perform CFD simulations using the smoothed-surface meshes.

Fig. 6 shows three alternative visualizations of a portion of the meshed geometry and provides a visual representation of the mesh resolution and refinement near surface boundaries.

Table 2
Parameters used in the STAR-CCM + mesh generation algorithm.

Parameter	Value
Base size	0.00001
Polynomial edge size	4–10% of base size
Surface grow rate	1.3
Number of boundary layers	2
Thickness of boundary layers	3% of base size
Minimum distance in the gap	10% of polynomial edge size

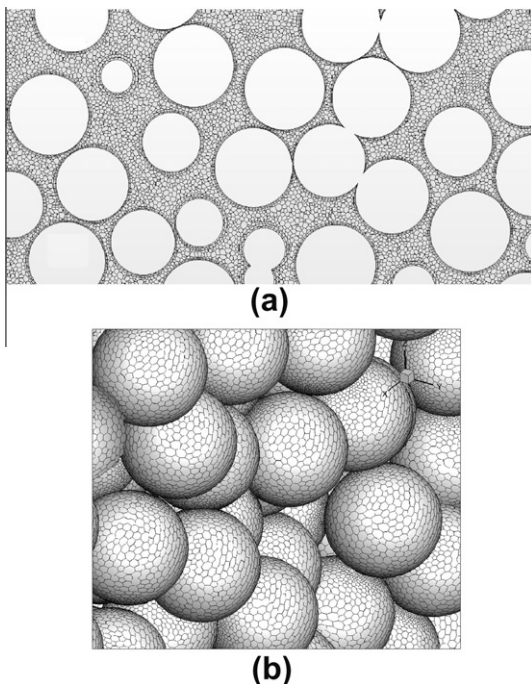


Fig. 6. Two visualizations of a portion of the smoothed-surface unstructured mesh: (a) a portion of the mesh in 2D; (b) meshed beads surfaces.

Table 3
Model configuration parameters and boundary conditions.

Parameter	Symbol(units)	Value
Bead diameter	d (mm)	0.5
Column diameter	D (mm)	8.8
Column length	L (mm)	12.8
Bed porosity	ε	0.4267
Volumetric flow rate	Q (kg/s)	2.771×10^{-5}
	Q (ml/hr)	100.0
Fluid density	ρ (kg/m ³)	997.561
Fluid dynamic viscosity	μ (pa-s)	8.887×10^{-4}

2.3.5. CFD parameters and boundary conditions

For the CFD simulations, the flow was assumed to be isothermal and incompressible with physical properties of water defined in Table 3. The dimensions and boundary conditions for the simulated system were specified to match the experimental conditions, also shown in Table 3. At the inlet of the bed, a fixed flow-rate of 100 ml/hr was specified. The outlet boundary is defined as a specified pressure condition. The wall of the tube and surfaces of the polystyrene beads are treated as “no-slip” boundaries. The Darcy flux for this system is $q = Q/(\pi(D/2)^2) = 1.64$ m/hr, and the average pore velocity is $v = q/\varepsilon = 3.85$ m/hr. The grain-scale Reynolds number can be calculated as $Re = v^* \rho^* d / \mu = 0.60$, which is in the laminar flow regime in which viscous forces predominate [76].

3. Results

In this section, simulated velocity fields from the two CFD codes are presented, compared to each another, and to the MRI measured velocity field. First we present macroscopic measures: (1) global and local mass balance checks; (2) grid type and resolution independence check; and (3) global porosity and pressure drop (permeability) calculations. Subsequently we present analyses of point-by-point comparison of simulated and experimental pore-scale velocity values.

3.1. Mesh independence check

Mesh independence checks were carried out among different unstructured smoothed-surface meshes generated in STAR-CCM+. During this procedure three different cell types were tested: hexahedral cells, polyhedral cells and tetrahedral cells. Geometries near the sphere surfaces are meshed using a prism layer, which is a layer of cells extending from the surface (see Section 2.3.4). Parameters used in the mesh generation (Table 2) were selected considering both computational accuracy and efficiency. The general strategy during meshing was to use extruded cells whenever possible, and full cells otherwise. By using various combinations of parameters, the numbers of total cells for each mesh were different (15 M for hexahedral mesh, 7 M and 30 M for polyhedral mesh, 20 M for tetrahedral mesh). Due to the mesh resolution, the porosity of the simulated packed-bed varied slightly. The pressure drop across the bead column was calculated and compared among different meshes in this procedure, which will be explained in Section 3.2. These grid convergence studies were for porosity and resistance estimations in flow simulation studies only. Additional resolution may be required to adequately represent tracer migration in transport simulations, which are not considered here.

3.2. Global and local mass balance

Both the simulated and experimental velocity fields exhibited good mass conservation both globally (over the entire column) and for each transverse slice of voxels. The nominal imposed flux

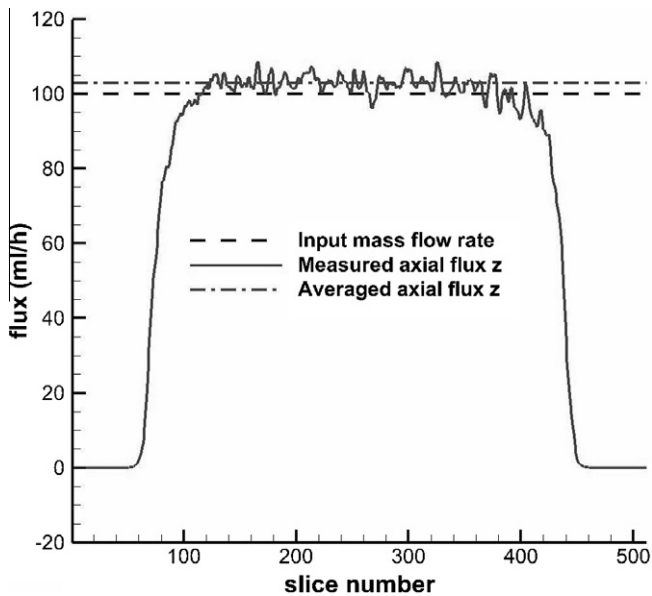


Fig. 7. Slice-by-slice average flux computed from experimental axial velocities.

through the experimental system was 100 ml/hr. MRI-measured axial velocity components were summed over all voxels in each slice; results are shown in Fig. 7. Near both ends of the column, the MRI data is compromised by the inhomogeneity of the radio-frequency excitation magnetic field near the r.f. coil ends and the resulting data are not used in the analysis, although they are shown in Fig. 7 for completeness. In the central portion of the column (at slice #320), the average sum of the axial velocities multiplied by the voxel face area of $39.06 \mu\text{m} \times 39.06 \mu\text{m}$ is used to calculate a mean flux of 98.1 ml/hr, a difference of -1.9% from the imposed flux. As can be seen in Fig. 7, the slice-by-slice estimates of local flux are reasonably consistent, varying around the mean value by approximately $\pm 4\%$.

The mass balance achieved by the numerical simulation is even tighter, with an average error in the mass flow rate of only -0.19%

and variations around the mean on a slice-by-slice basis of much less than 1%.

Based on this analysis, we conclude that both the simulated and experimental velocity fields provide good mass balance.

3.3. Global porosity and pressure drop

The porosity of the smoothed-surface simulated system (the summed volume of solid mesh elements divided by the total volume of the system) is 0.4267, which closely matches the experimental porosity derived from the MRI-measured geometry of 0.43. Dixon [77] developed an empirical correlation relationship for optimal packing of uniform spheres of diameter d within a column of diameter D that accounts for wall effects; application of Dixon's relationship gives an expected porosity of 0.4042, which reasonably matches the experimental and simulation values (5% difference).

The expected pressure drop across the polystyrene bead column can be estimated for a packed bed of uniform spheres based on relationships given in [78,79]; these relationships were also used by [38] to validate their CFD computations. The relationship for pressure drop as given by [78] using the approach of [79] to correct for wall effects, gives an estimated pressure drop of 14.29 Pa for the conditions of the experiment, whereas the simulated pressure drop for the smoothed surface mesh was 13.65 Pa, a difference of only 4.5%. The corresponding calculated pressure drops from the voxel mesh simulations were 13.32 Pa (40-micron) and 13.19 Pa (20-micron), respectively, with differences less than 8% compared to the correlation in [78,79]. Compared to the pressure drop calculated from the well-known Carmen–Kozeny equation [80,81] (13.19 Pa), the difference is within 1%. The hydraulic conductivity of the packed bed, based on the simulated pressure drop for the smoothed surface mesh, is $4.2 \times 10^{-1} \text{ cm/s}$, which is in the typical range observed for clean well-sorted sand (see Table 5.5.1 of [82]). Thus the simulated macroscopic behavior is consistent with that expected based on established empirical relationships for packed bed systems.

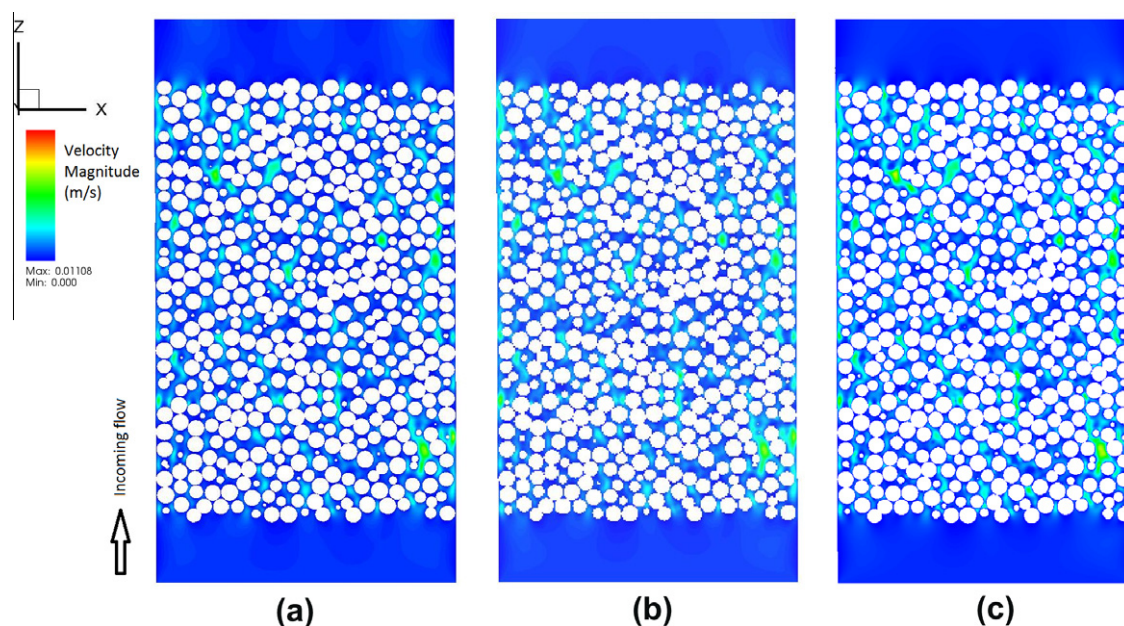


Fig. 8. Color contour plots of velocity magnitude (m/s) along the center axial plane of the simulated datasets: (a) STAR-CCM+ computation using a smoothed-surface unstructured mesh fitted to extracted spheres, (b) TETHYS simulation using a cubic mesh based on voxels (40-micron resolution) directly imaged using MRI and (c) TETHYS simulation using a cubic mesh based on voxels (20-micron resolution) directly imaged using MRI. Color contour levels are the same for all three simulations.

3.4. Velocity distribution – comparison between two meshes

Contour plots of the computed velocity magnitude along an axial plane through the bead pack, obtained using STAR-CCM+ with the smoothed-surface unstructured mesh and TETHYS with the 40-micron voxel mesh, are shown in Fig. 8. Very similar flow patterns are observed, indicating that the stair-step mesh does not significantly degrade the solution in terms of local velocities. We note that the highest velocities are observed in the near-wall region, where the porosity is highest and spheres tend to form a more ordered pattern due to interaction with the column walls. Fig. 9 shows the average axial velocity computed in concentric rings of the bead pack as a function of radial distance. The higher velocities near the wall are clearly indicated by this figure, and are consistent with observations of previous investigators (see discussion in [83] and references cited therein). Also note that the averaged velocities calculated from the voxel mesh simulation are generally higher than the smoothed-surface mesh simulation, which could be due to the accelerated flow near the sharp edges of the stepped mesh.

3.5. Velocity distribution – comparison with experimental data

Here we compare the results of the two simulation methods with MRV measurements of pore-scale velocity. Fig. 10 shows a selected slice (#320) through the three-dimensional system, with color contours of velocity magnitude in the pore spaces, for the experimental system and two model systems (STAR-CCM+ with smoothed-surface mesh and TETHYS with 40 micron voxel mesh).

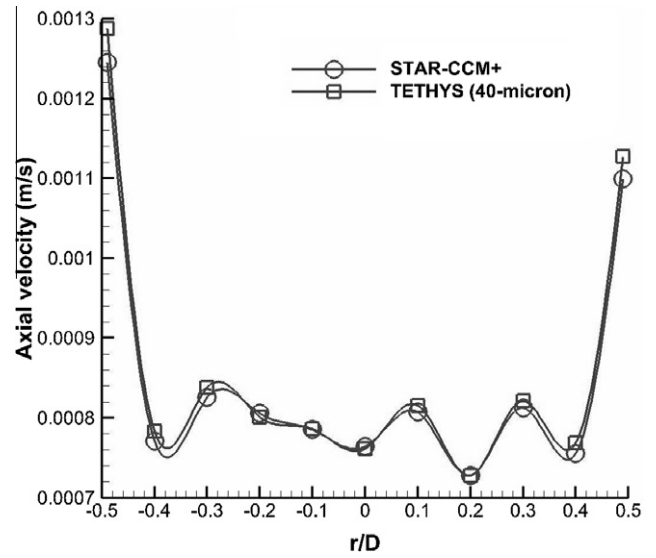


Fig. 9. The average axial velocity profiles computed in concentric rings of the bead pack, as a function of radial distance.

The spatial patterns of velocity compare very favorably among the three cases, but close inspection reveals some significant differences in point-by-point values, especially for the highest velocities. Fig. 11 shows an expanded view of the subregion of slice #320 indicated by the black box in Fig. 10b. The two simulation methods compare exceptionally well, even in terms of point values. The experimental data compares reasonably well to the simulated data

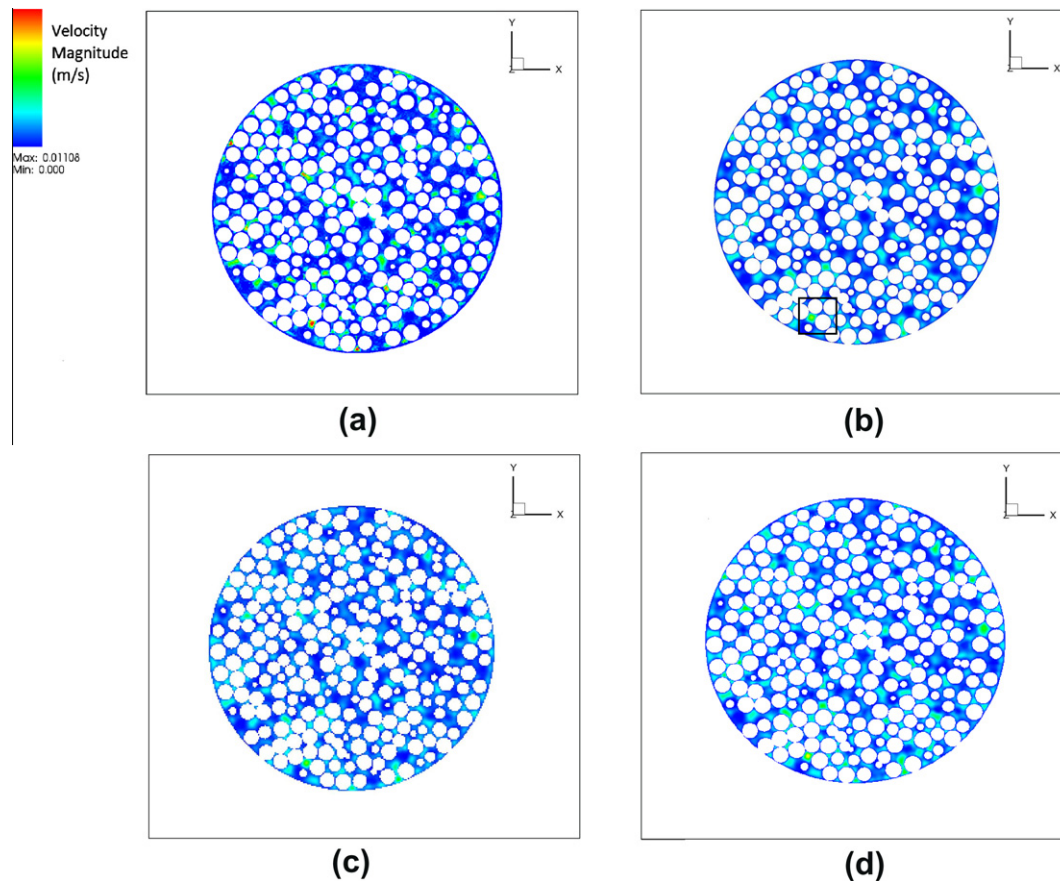


Fig. 10. Color contour plots of velocity in slice #320 (in the middle of the packed-bed at Z = 6.4 mm): (a) experimental data; (b) STAR-CCM+ simulation; (c) TETHYS 40 μm simulation; d) TETHYS 20 μm simulation.

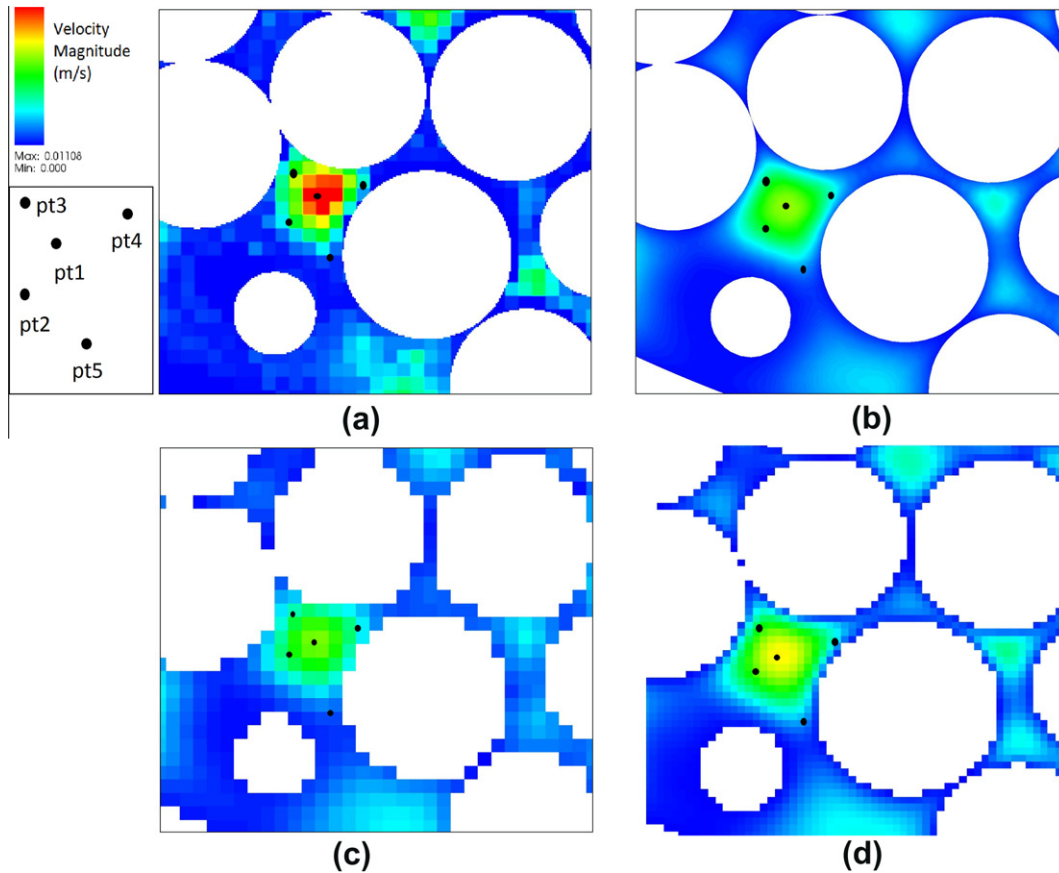


Fig. 11. Magnified visualization of velocity fields in the subregion of slice #320 indicated by a black box in Fig. 10b: (a) experimental; (b) simulated (STAR-CCM+); (c) simulated (TETHYS 40-micron mesh); and (d) simulated (TETHYS 20-micron mesh). Color scales are the same in all four images. The locations of the five points are fixed for comparison purposes (see Table 4). Note that cases a, c and d all show direct plots of voxel-based data, but case b is contoured values from an irregular grid and therefore may appear artificially smooth due to the contouring algorithm used by visualization software. Velocity magnitudes range on the same linear color scale in all four images, from zero (blue) to 0.01106 m/s (red).

Table 4

Comparison of experimental and simulated values of axial and transverse velocity components at the selected locations in slice #320 indicated in Fig. 11.

	MRI (m/s)	STAR-CCM+ (m/s)	Err% (MRI vs STAR-CCM+)	TETHYS (m/s)		Err% (STAR-CCM + vs TETHYS)	
				20 μ m	40 μ m	20 μ m	40 μ m
<i>Vz (axial)</i>							
Point 1	0.011496	0.007142	37.87	0.007038	0.006622	1.46	7.28
Point 2	0.009879	0.005837	40.92	0.005942	0.005667	1.80	2.91
Point 3	0.007748	0.005186	33.07	0.005013	0.004774	3.33	7.95
Point 4	0.002219	0.00186	16.17	0.002042	0.001958	9.78	5.29
Point 5	0.000523	0.000425	18.78	0.000431	0.000407	1.41	4.31
<i>Vx (transverse)</i>							
Point 1	-0.000958	-0.00055	74.35	-0.000566	-0.000584	2.91	6.14
Point 2	-0.000838	-0.000542	54.50	-0.000539	-0.000514	0.55	5.14
Point 3	-0.000739	-0.000636	16.14	-0.000641	-0.000622	0.78	2.23
Point 4	-0.000107	-0.000096	11.13	-0.000094	-0.000102	2.08	5.77
Point 5	0.000089	0.000088	1.12	0.000093	0.000090	5.68	1.81
<i>Vy (transverse)</i>							
Point 1	-0.000074	-0.000182	59.32	-0.000185	-0.000177	1.65	2.63
Point 2	-0.000071	-0.000148	51.68	-0.000143	-0.000139	3.38	6.30
Point 3	-0.000779	-0.000097	19.90	-0.000110	-0.000110	13.4	12.98
Point 4	-0.001096	-0.000942	16.28	-0.000931	-0.000906	1.17	3.81

given the measurement uncertainty in the experimental data of ± 0.44 mm/s.

Table 4 provides a tabular listing of actual values of three velocity components (axial and two transverse directions) at the five

points identified in Fig. 11, which lie within the central high-velocity pore. At each of the five points, the measured axial component of velocity (in the direction of average flow) is significantly higher than both of the simulated values, with errors ranging from 16% to

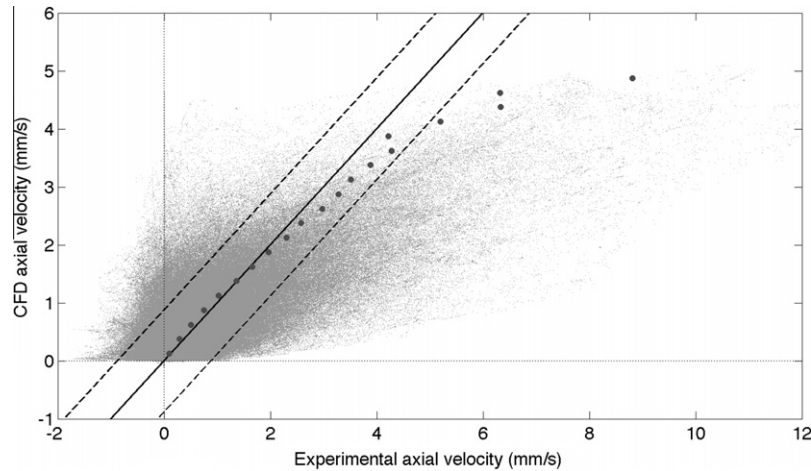


Fig. 12. Scatter plot of axial velocity values computed using the CFD method with smoothed-surface mesh (vertical axis) versus corresponding experimentally measured values (horizontal axis), for the complete dataset of approximately 21 million voxels. The experimental values were spatially interpolated onto the nearest CFD mesh points to produce the comparison. The 1:1 line ($y = x$; perfect match between experiment and simulation) is indicated by a solid black line; dashed black lines indicate plus/minus two standard deviations of the derived experimental error distribution. The gray solid circles are averages of experimental velocities corresponding to simulated velocities binned in 0.25 mm/s intervals.

40%. The values predicted by the two different simulation methods are much closer to each other, with differences ranging from 2% to 8%.

The results shown in Fig. 10, Fig. 11, and Table 4 for slice #320 are uniformly characteristic of other slices in the experimental and simulated datasets. In general, the experimental data exhibit consistently larger amplitudes of high velocity than either simulation method. This is clearly indicated by Fig. 12, which shows a scatter plot of simulated versus experimental velocities for the entire set of approximately 21 million experimental voxels in the dataset. The 1:1 line ($y = x$), indicative of a perfect match between experiment and simulation, is shown. At low velocities the distribution of velocities obtained experimentally compares well with the simulation, in that the means of the experimental values (gray dots) lie close to the 1:1 line and most of the data points fall within two standard deviations of the experimental uncertainty (± 0.88 mm/s) of the 1:1 line (see dashed lines in Fig. 12). Note that this experimental uncertainty was independently estimated from a separate experiment as described above (Section 2.2.b). However, at higher velocities there is a clear systematic bias as indicated by the gray dots (means of the experimental values). This systematic bias at higher velocities may be explained in part by adjustments made to the MRV velocities to account for the effect of amplifier offset in the gradient amplitude over the course of the experimental period. In MRV the reference velocity rescaling is usually determined by normalizing with an identical non-flowing data set. However, the long duration of these MRI experiments required to obtain sufficient signal-to-noise ratio (7 days) led to significant gradient amplifier offset drift. Although the gradient offset is of much smaller magnitude than the spatial or velocity magnetic field encoding gradients and does not impact those measurements, it precludes determination of a single reference phase over the 7-day period. Therefore, in this case the velocities were instead rescaled so as to fix the total mass flux to 100 ml/hr in each slice, which was independently validated to be the volumetric flow rate. A very large percentage of the velocity data points have low velocity, and this rescaling had minor impact on those points relative to the spread in the data associated with experimental uncertainty. However, for the relatively few data points with large velocity, this rescaling had a greater impact and is evidenced as bias in the scatter plot (Fig. 12). While this provides a partial explanation as to why the apparent errors are larger for the higher velocities, there may be

other sources of error in either the simulation or experimental data that also contribute to these discrepancies. Further work is needed to confirm the accuracy of the simulated and experimental velocities at the upper end of the distribution. One potential approach will be to perform physical and numerical tracer experiments, and compare breakthrough curves from each method; high velocities should have an impact on early arrival times and such a study would provide further evidence as to the magnitude and source of errors in either experimental or simulated velocities.

The univariate distributions (histograms) of all the velocities in both the experimental data set and the simulation data set for slices 101:420 are shown in Fig. 13. A significant number of negative axial velocities are apparent in the experimental data, whereas the simulation data contains only a small fraction. Under laminar flow conditions studied here, we would not expect to see extensive eddy formation, which would be the primary cause of negative axial velocities. The experimental data also shows a significant number of faster velocities than the maximum velocity seen in the

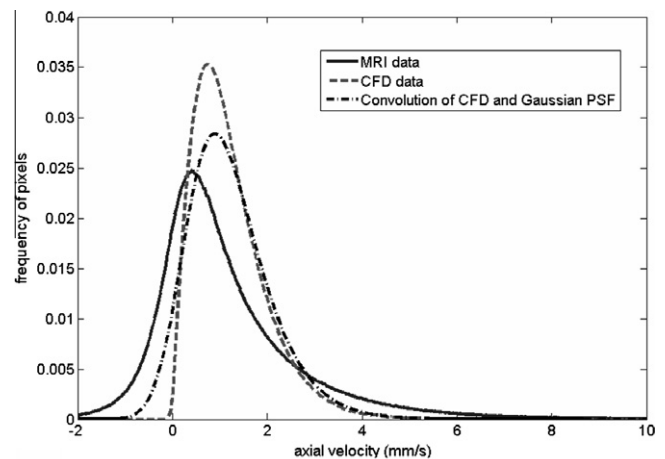


Fig. 13. The distribution of velocities in the CFD simulation is shown in red. The distribution of velocities in the MRI experimental data set is shown by the solid line. The CFD data convoluted with a Gaussian point spread function GPSF with a variance of 0.2 mm/s is shown as a dashed-dot line. The dashed-dot line compares very well with the measured distribution of velocities, the solid line.

simulation. As discussed above with reference to Fig. 12, the primary source of this broader distribution in the experimental data is due to the uncertainty involved in the experimental measurement of the velocity, as described in Fig. 1. The convolution of the distribution of velocities obtained in the simulation (dashed line in Fig. 13) with a GPSF with a variance of $\sigma^2 = 0.19 \text{ mm}^2/\text{s}^2 = (0.44 \text{ mm/s})^2$ is shown in black in Fig. 13 which agrees more closely with the experimentally obtained data.

4. Conclusions

We have presented an experimental validation of CFD-based simulations of pore-scale single-phase flow in a packed bed consisting of uniform polystyrene beads, using MRI measurements of pore-scale velocity. The results demonstrate that the simulated and experimental velocity fields exhibit very similar spatial patterns. Two primary differences were observed between the simulated and experimental velocities: (1) the experimental data exhibited a larger spread in velocities, which could be largely explained by quantifiable experimental noise (Fig. 13); and (2) in point-to-point velocity comparisons the largest discrepancies occurred at high velocity locations (e.g., centers of pore throats), which could be in part explained by the method used to adjust for the background phase shift given the gradient amplifier offset drift during the course of the MRV experiments. Although further work is needed to further resolve these differences, the results demonstrate that given contemporary parallel computing capabilities, it is possible to accurately simulate Navier–Stokes flow in a column with centimeter-scale overall dimensions at pore-scale resolution of geometry and velocity. This provides substantiation for studies that rely on accurate pore-scale velocity fields as the basis for simulations of other porous media processes such as dispersion, mixing-controlled transport, colloid and microbial transport, etc. We determined that the simulated velocity fields were largely consistent with the MRI-measured velocities, in terms both of overall spatial patterns and point-to-point velocity values, when the impacts of signal to noise limited velocity resolution on the MRI measurements were properly accounted for. Some skewing of the highest velocities was present in the experimental data due to difficulties in determining the exact velocity shift (gradient induced phase shift) over the course of the MRV experiments. The next step in this line of research will be to perform comparisons of simulated and experimental tracer transport studies to provide further assessment of the validity of CFD-simulated velocity fields.

We also found, somewhat surprisingly, that simulation results obtained using a cubic voxel mesh based directly on the MRI geometry measurements (at both 20- and 40-micrometer resolutions) differed only slightly from simulation results obtained using a much more complex and highly-resolved smoothed-surface unstructured mesh. This suggests that, at least for simulation of pore-scale velocities (and possibly for simulation of velocity dependent quantities such as axial dispersion coefficients), it is not necessary to invest effort in development of more sophisticated meshes. However, we note this conclusion likely does not extend to simulations of pore-scale processes that strongly depend on grain surface area and geometry such as chemical sorption, intragranular diffusion, and colloid deposition.

Finally, this combined experimental and numerical dataset provides opportunities for future benchmarking and cross-validation studies. Here we compared results only with a CFD-based pore-scale simulation, but it would be of significant interest to simulate the same system using other pore-scale simulation approaches such as SPH, pore-network, and Lattice Boltzmann methods. To facilitate access and use by other investigators, we are placing the simulated and experimental velocity data into the

PoreScaleBenchmark project environment (<http://porescalebenchmark.pbworks.com/w/page/47913874/PoreScaleBenchmark>).

Acknowledgments

Research at Pacific Northwest National Laboratory (PNNL) was supported by the U. S. Department of Energy (DOE) Office of Biological and Environmental Research (BER), Subsurface Biogeochemical Research program, through PNNL's Subsurface Science Scientific Focus Area project. Research at Montana State University was supported by grant number DE-FG02-07-ER-64416 from the DOE-BER Environmental Remediation Sciences Program. Computations described here were performed using computational facilities of the Environmental Molecular Sciences Laboratory (EMSL), a national scientific user facility sponsored by DOE-BER and located at PNNL, the National Energy Research Supercomputing Center (NERSC), which is supported by the DOE Office of Science under Contract No. DE-AC02-05CH11231, and the PNNL Institutional Computing (PIC) facility. PNNL is operated for the DOE by Battelle Memorial Institute under Contract No. DE-AC05-76RL01830.

References

- [1] Le Borgne T, Dentz M, Davy P, Bolster D, Carrera J, de Dreuzy JR. Persistence of incomplete mixing: a key to anomalous transport. *Phys Rev E* 2011;84. <http://dx.doi.org/10.1103/PhysRevE.84.015301>. doi: Artn 015301.
- [2] Dentz M, Le Borgne T, Englert A, Bijeljic B. Mixing, spreading and reaction in heterogeneous media: a brief review. *J Contam Hydrol* 2011;120–21:1–17. <http://dx.doi.org/10.1016/j.jconhyd.2010.05.002>.
- [3] Battiato I, Tartakovsky DM, Tartakovsky AM, Scheibe T. On breakdown of macroscopic models of mixing-controlled heterogeneous reactions in porous media. *Adv Water Resour* 2009;32:1664–73. <http://dx.doi.org/10.1016/j.advwatres.2009.08.008>.
- [4] Tartakovsky AM, Redden G, Lichtner PC, Scheibe TD, Meakin P. Mixing-induced precipitation: experimental study and multiscale numerical analysis. *Water Resour Res* 2008;44. <http://dx.doi.org/10.1029/2006WR005725>.
- [5] Cirpka OA, Schwede RL, Luo J, Dentz M. Concentration statistics for mixing-controlled reactive transport in random heterogeneous media. *J Contam Hydrol* 2008;98:61–74. <http://dx.doi.org/10.1016/j.jconhyd.2008.03.005>.
- [6] Luo J, Dentz M, Carrera J, Kitanidis P. *Water Resour Res* 2008;44. <http://dx.doi.org/10.1029/2006wr005658>. doi: Artn W02416.
- [7] Tartakovsky AM, Tartakovsky GD, Scheibe TD. Effects of incomplete mixing on multicomponent reactive transport. *Adv Water Resour* 2009;32:1674–9. <http://dx.doi.org/10.1016/j.advwatres.2009.08.012>.
- [8] Molins S, Trebotich D, Steefel CI, Shen CP. An investigation of the effect of pore scale flow on average geochemical reaction rates using direct numerical simulation. *Water Resour Res* 2012;48. <http://dx.doi.org/10.1029/2011wr011404>.
- [9] Tartakovsky AM, Scheibe TD, Meakin P. Pore-scale model for reactive transport and biomass growth. *J Porous Media* 2009;12:417–34. <http://dx.doi.org/10.1615/JPorMedia.v12.i5.30>.
- [10] Xu ZJ, Meakin P, Tartakovsky A, Scheibe TD. Dissipative-particle-dynamics model of biofilm growth. *Phys Rev E* 2011;83. <http://dx.doi.org/10.1103/PhysRevE.83.066702>. doi: Artn 066702.
- [11] Celia MA, Dahle HK, Hassanizadeh SM. Dynamic pore-scale network models for two-phase flow in porous media. *Comput Methods Water Resour* 2000;Vols 1 and 2:217–23.
- [12] Blunt MJ. Flow in porous media – pore-network models and multiphase flow. *Curr Opin Colloid In* 2001;6:197–207. [http://dx.doi.org/10.1016/S1359-0294\(01\)00084-X](http://dx.doi.org/10.1016/S1359-0294(01)00084-X).
- [13] Valvatne PH, Piri M, Lopez X, Blunt MJ. Predictive pore-scale modeling of single and multiphase flow. *Transport Porous Med* 2005;58:23–41. <http://dx.doi.org/10.1007/s11242-004-5468-2>.
- [14] Joekar-Niasar V, Hassanizadeh SM. Specific interfacial area: the missing state variable in two-phase flow equations? *Water Resour Res* 2011;47:W05513. <http://dx.doi.org/10.1029/2010WR009291>.
- [15] Piri M, Blunt MJ. Three-dimensional mixed-wet random pore-scale network modeling of two- and three-phase flow in porous media. I. Model description. *Phys Rev E* 2005;71. <http://dx.doi.org/10.1103/PhysRevE.71.026301>. doi: Artn 026301.
- [16] Kang QJ, Lichtner PC, Zhang DX. An improved lattice Boltzmann model for multicomponent reactive transport in porous media at the pore scale. *Water Resour Res* 2007;43. <http://dx.doi.org/10.1029/2006wr005551>. doi: W12s14.
- [17] Kang QJ, Lichtner PC, Janecky DR. Lattice Boltzmann method for reacting flows in porous media. *Adv Appl Math Mech* 2010;2:545–63. <http://dx.doi.org/10.4208/aamm.10-10S02>.
- [18] Kang QJ, Lichtner PC, Viswanathan HS, Abdel-Fattah AI. Pore scale modeling of reactive transport involved in geologic CO₂ sequestration. *Transport Porous Med* 2010;82:197–213. <http://dx.doi.org/10.1007/s11242-009-9443-9>.

- [19] Van Leemput P, Vandekerckhove C, Vanroose W, Roose D. Accuracy of hybrid lattice Boltzmann/finite difference schemes for reaction–diffusion systems. *Multiscale Model Simulat* 2007;6:838–57. <http://dx.doi.org/10.1137/060675113>.
- [20] Sukop MC, Huang H, Lin CL, Deo MD, Oh K, Miller JD. Distribution of multiphase fluids in porous media: comparison between lattice Boltzmann modeling and micro-X-ray tomography. *Phys Rev E* 2008;77. <http://dx.doi.org/10.1103/PhysRevE.77.026710>.
- [21] Huang HB, Lu XY, Sukop MC. Numerical study of lattice Boltzmann methods for a convection–diffusion equation coupled with Navier–Stokes equations. *J Phys A-Math Theor* 2011;44. <http://dx.doi.org/10.1088/1751-8113/44/5/055001>. doi: 055001.
- [22] Maier RS, Kroll DM, Bernard RS, Howington SE, Peters JF, Davis HT. Hydrodynamic dispersion in confined packed beds. *Phys Fluids* 2003;15:3795–815. <http://dx.doi.org/10.1063/1.1624836>.
- [23] Maier RS, Kroll DM, Bernard RS, Howington SE, Peters JF, Davis HT. Pore-scale simulation of dispersion. *Phys Fluids* 2000;12:2065–79. <http://dx.doi.org/10.1063/1.870452>.
- [24] Manz B, Gladden LF, Warren PB. Flow and dispersion in porous media: Lattice-Boltzmann and NMR studies. *Aiche J* 1999;45:1845–54. <http://dx.doi.org/10.1002/aic.690450902>.
- [25] Sullivan SP, Sederman AJ, Johns ML, Gladden LF. Verification of shear-thinning LB simulations in complex geometries. *J Non-Newton Fluid Mech* 2007;143:59–63. <http://dx.doi.org/10.1016/j.jnnfm.2006.12.008>.
- [26] He XY, Luo LS. Lattice Boltzmann model for the incompressible Navier–Stokes equation. *J Stat Phys* 1997;88:927–44. <http://dx.doi.org/10.1023/B:loss.0000015179.12689.E4>.
- [27] Chen S, Doolen GD. Lattice Boltzmann method for fluid flows. *Annu Rev Fluid Mech* 1998;30:329–64. <http://dx.doi.org/10.1146/annurev.fluid.30.1.329>.
- [28] Tartakovsky AM, Meakin P, Scheibe TD, West RME. Simulations of reactive transport and precipitation with smoothed particle hydrodynamics. *J Comput Phys* 2007;222:654–72. <http://dx.doi.org/10.1016/j.jcp.2006.08.013>.
- [29] Tartakovsky AM, Meakin P, Scheibe TD, Wood BD. A smoothed particle hydrodynamics model for reactive transport and mineral precipitation in porous and fractured porous media. *Water Resour Res* 2007;43. <http://dx.doi.org/10.1029/2005WR004770>.
- [30] Berry RA, Martineau RC, Wood TR. Particle-based direct numerical simulation of contaminant transport and deposition in porous flow. *Vadose Zone J* 2004;3:164–9. <http://dx.doi.org/10.2136/vzj2004.1640>.
- [31] Herrera PA, Valocchi AJ, Beckie RD. A multidimensional streamline-based method to simulate reactive solute transport in heterogeneous porous media. *Adv Water Resour* 2010;33:711–27. <http://dx.doi.org/10.1016/j.advwatres.2010.03.001>.
- [32] Liu MB, Liu GR. Smoothed particle hydrodynamics (SPH): an overview and recent developments. *Arch Comput Methods Eng* 2010;17:25–76. <http://dx.doi.org/10.1007/s11831-010-9040-7>.
- [33] Logtenberg SA, Dixon AG. Computational fluid dynamics studies of the effects of temperature-dependent physical properties on fixed-bed heat transfer. *Ind Eng Chem Res* 1998;37:739–47. <http://dx.doi.org/10.1021/ie970382g>.
- [34] Morais AF, Seybold H, Herrmann HJ, Andrade JS. Non-Newtonian fluid flow through three-dimensional disordered porous media. *Phys Rev Lett* 2009;103. <http://dx.doi.org/10.1103/PhysRevLett.103.194502>. doi: 194502.
- [35] Dixon AG, Nijemeisland M. CFD as a design tool for fixed-bed reactors. *Ind Eng Chem Res* 2001;40:5246–54. <http://dx.doi.org/10.1021/ie01035a>.
- [36] Nijemeisland M, Dixon AG. CFD study of fluid flow and wall heat transfer in a fixed bed of spheres. *Aiche J* 2004;50:906–21. <http://dx.doi.org/10.1002/aic.10089>.
- [37] Zaretskiy Y, Geiger S, Sorbie K, Forster M. Efficient flow and transport simulations in reconstructed 3D pore geometries. *Adv Water Resour* 2010;33:1508–16. <http://dx.doi.org/10.1016/j.advwatres.2010.08.008>.
- [38] Eppinger T, Seidler K, Kraume M. DEM-CFD simulations of fixed bed reactors with small tube to particle diameter ratios. *Chem Eng J* 2011;166:324–31. <http://dx.doi.org/10.1016/j.cej.2010.10.053>.
- [39] Cardenas MB. Three-dimensional vortices in single pores and their effects on transport. *Geophys Res Lett* 2008;35. <http://dx.doi.org/10.1029/2008gl035343>. doi: L18402.
- [40] Gielen T, Hassanizadeh SN, Celia MA, Dahle HK, Leijnse A. A pore-scale network approach to investigate dynamic effects in multiphase flow. *Comput Methods Water Resour* 2004;Vols 1 and 2. 55:83–94.
- [41] Celia MA, Reeves PC, Ferrand LA. Recent advances in pore scale models for multiphase flow in porous-media. *Rev Geophys* 1995;33:1049–57. <http://dx.doi.org/10.1029/95rg00248>.
- [42] Li L, Peters CA, Celia MA. Upscaling geochemical reaction rates using pore-scale network modeling. *Adv Water Resour* 2006;29:1351–70. <http://dx.doi.org/10.1016/j.advwatres.2005.10.011>.
- [43] Blunt MJ, Jackson MD, Piri M, Valvatne PH. Detailed physics, predictive capabilities and macroscopic consequences for pore-network models of multiphase flow. *Adv Water Resour* 2002;25:1069–89. [http://dx.doi.org/10.1016/s0309-1708\(02\)00049-0](http://dx.doi.org/10.1016/s0309-1708(02)00049-0).
- [44] Blunt M, King P. Macroscopic parameters from simulations of pore scale flow. *Phys Rev A* 1990;42:4780–7. <http://dx.doi.org/10.1103/PhysRevA.42.4780>.
- [45] Bijeljic B, Blunt MJ. Pore-scale modeling and continuous time random walk analysis of dispersion in porous media. *Water Resour Res* 2006;42. <http://dx.doi.org/10.1029/2005wr004578>.
- [46] Rhodes ME, Bijeljic B, Blunt MJ. A rigorous pore-to-field-scale simulation method for single-phase flow based on continuous-time random walks. *Spe J* 2009;14:88–94. <http://dx.doi.org/10.2118/106434-PA>.
- [47] Al-Raoush RI, Willson CS. A pore-scale investigation of a multiphase porous media system. *J Contam Hydrol* 2005;77:67–89. <http://dx.doi.org/10.1016/j.jconhyd.2004.12.001>.
- [48] Gunjal PR, Ranade VV, Chaudhari RV. Computational study of a single-phase flow in packed beds of spheres. *Aiche J* 2005;51:365–78. <http://dx.doi.org/10.1002/aic.10314>.
- [49] Schaap MG, Porter ML, Christensen BSB, Wildenschild D. Comparison of pressure-saturation characteristics derived from computed tomography and lattice Boltzmann simulations. *Water Resour Res* 2007;43. <http://dx.doi.org/10.1029/2006wr005730>.
- [50] Callaghan PT. *Translational dynamics and magnetic resonance: principles of pulsed gradient spin echo NMR*. Oxford: Oxford University Press; 2011.
- [51] Seymour JD, Callaghan PT. Generalized approach to NMR analysis of flow and dispersion in porous media. *Aiche J* 1997;43:2096–111. <http://dx.doi.org/10.1002/aic.690430817>.
- [52] Stapf S, Packer KJ, Graham RG, Thovert JF, Adler PM. Spatial correlations and dispersion for fluid transport through packed glass beads studied by pulsed field-gradient NMR. *Phys Rev E* 1998;58:6206–21. <http://dx.doi.org/10.1103/PhysRevE.58.6206>.
- [53] Johns ML, Sederman AJ, Bramley AS, Gladden LF, Alexander P. Local transitions in flow phenomena through packed beds identified by MRI. *Aiche J* 2000;46:2151–61. <http://dx.doi.org/10.1002/aic.690461108>.
- [54] Seto K, Hollenshead JT, Watson JAT, Chang CTP, Slattery JC. Determination of permeability distributions using NMR velocity imaging. *Transport Porous Med* 2001;42:351–88. <http://dx.doi.org/10.1023/A:1006737103710>.
- [55] Anadon LD, Sederman AJ, Gladden LF. Mechanism of the trickle-to-pulse flow transition in fixed-bed reactors. *AIChE J* 2006;52:1522–32. <http://dx.doi.org/10.1002/aic.10737>.
- [56] Sankey MH, Holland DJ, Sederman AJ, Gladden LF. Magnetic resonance velocity imaging of liquid and gas two-phase flow in packed beds. *J Magn Reson* 2009;196:142–8. <http://dx.doi.org/10.1016/j.jmr.2008.10.021>.
- [57] Seymour JD, Gage JP, Codd SL, Gerlach R. Anomalous fluid transport in porous media induced by biofilm growth. *Phys Rev Lett* 2004;93. <http://dx.doi.org/10.1103/PhysRevLett.93.198103>. doi: 198103.
- [58] Seymour JD, Codd SL, Gjersten EL, Stewart PS. Magnetic resonance microscopy of biofilm structure and impact on transport in a capillary bioreactor. *J Magn Reson* 2004;167:322–7. <http://dx.doi.org/10.1016/j.jmr.2004.01.009>.
- [59] Seymour JD, Gage JP, Codd SL, Gerlach R. Magnetic resonance microscopy of biofouling induced scale dependent transport in porous media. *Adv Water Resour* 2007;30:1408–20. <http://dx.doi.org/10.1016/j.advwatres.2006.05.029>.
- [60] Hoskins BC, Fevang L, Majors PD, Sharma MM, Georgiou G. Selective imaging of biofilms in porous media by NMR relaxation. *J Magn Reson* 1999;139:67–73. <http://dx.doi.org/10.1006/jmr.1999.1747>.
- [61] von der Schulenburg DAG, Akpa BS, Gladden LF, Johns ML. Non-invasive mass transfer measurements in complex biofilm-coated structures. *Biotechnol Bioeng* 2008;101:602–8. <http://dx.doi.org/10.1002/bit.21913>.
- [62] Bijeljic B, Mantle MD, Sederman AJ, Gladden LF, Papanthanasios TD. Slow flow across macroscopically semi-circular fibre lattices and a free-flow region of variable width-visualisation by magnetic resonance imaging. *Chem Eng Sci* 2004;59:2089–103. <http://dx.doi.org/10.1016/j.ces.2004.02.007>.
- [63] Elkins CJ, Alley MT. Magnetic resonance velocimetry: applications of magnetic resonance imaging in the measurement of fluid motion. *Exp Fluids* 2007;43:823–58. <http://dx.doi.org/10.1007/s00348-007-0383-2>.
- [64] Yiallourou TI, Asboth L, Kroeger J-R, Maintz D, Bunck AC, Stergiopoulos N. Quantitative comparison of 4D MRI flow measurements to 3D computational fluid dynamics simulation of cerebrospinal fluid movement in the spinal subarachnoid space. In: 10th International Workshop on Biomedical Engineering. Kos Island, Greece: IEEE; 2011. <http://dx.doi.org/10.1109/IWBE.2011.6079027>.
- [65] de Rochefort L, Vial L, Fodil R, Maitre X, Louis B, Isabey D. In vitro validation of computational fluid dynamic simulation in human proximal airways with hyperpolarized (³He) magnetic resonance phase-contrast velocimetry. *J Appl Physiol* 2007;102:2012–23. <http://dx.doi.org/10.1152/japplphysiol.01610.2005>.
- [66] Mantle MD, Sederman AJ, Gladden LF. Single- and two-phase flow in fixed-bed reactors: MRI flow visualisation and lattice-Boltzmann simulations. *Chem Eng Sci* 2001;56:523–9. [http://dx.doi.org/10.1016/s0009-2509\(00\)00256-6](http://dx.doi.org/10.1016/s0009-2509(00)00256-6).
- [67] Suekane T, Yokouchi Y, Hirai S. Inertial flow structures in a simple-packed bed of spheres. *Aiche J* 2003;49:10–7. <http://dx.doi.org/10.1002/aic.690490103>.
- [68] Maier RS, Schure MR, Gage JP, Seymour JD. Sensitivity of pore-scale dispersion to the construction of random bead packs. *Water Resour Res* 2008;44. <http://dx.doi.org/10.1029/2006wr005577>.
- [69] Ferziger JH, Peric M. *Computational methods for fluid dynamics*. 3rd ed. Berlin: Springer-Verlag; 2001. ISBN 978-3-540-42074-3.
- [70] Patankar SV. *Numerical heat transfer and fluid flow*. New York: Hemisphere/McGraw-Hill; 1980. ISBN 0891165223.
- [71] Ghia U, Ghia KN, Shin CT. High-re solutions for incompressible-flow using the Navier stokes equations and a multigrid method. *J Comput Phys* 1982;48:387–411. [http://dx.doi.org/10.1016/0021-9991\(82\)90058-4](http://dx.doi.org/10.1016/0021-9991(82)90058-4).
- [72] Maier RS, Bernard RS. Lattice-Boltzmann accuracy in pore-scale flow simulation. *J Comput Phys* 2010;229:233–55. <http://dx.doi.org/10.1016/j.jcp.2009.09.013>.

- [73] Zick AA, Homsy GM. Stokes-flow through periodic arrays of spheres. *J Fluid Mech* 1982;115:13–26. <http://dx.doi.org/10.1017/s0022112082000627>.
- [74] Hill RJ, Koch DL, Ladd AJC. Moderate-Reynolds-number flows in ordered and random arrays of spheres. *J Fluid Mech* 2001;448:243–78. <http://dx.doi.org/10.1017/S0022112001005936>.
- [75] Sangani AS, Acrivos A. Slow flow past periodic arrays of cylinders with application to heat transfer. *Int J Multiph Flow* 1982;8:193–206. [http://dx.doi.org/10.1016/0301-9322\(82\)90029-5](http://dx.doi.org/10.1016/0301-9322(82)90029-5).
- [76] Dybbs A, Edwards R. A new look at porous media mechanics – darcy to turbulent. In: *Fundamentals of Transport Phenomena in Porous Media*. Zoetermeer, Netherlands: Martinus Nijhoff; 1984. p. 199–254. <http://dx.doi.org/10.1002/cnm.1630010513>.
- [77] Dixon AG. Correlations for wall and particle-shape effects on fixed-bed bulk voidage. *Can J Chem Eng* 1988;66:705–8. <http://dx.doi.org/10.1002/cjce.5450660501>.
- [78] Einfeld B, Schnitzlein K. The influence of confining walls on the pressure drop in packed beds. *Chem Eng Sci* 2001;56:4321–9. [http://dx.doi.org/10.1016/s0009-2509\(00\)00533-9](http://dx.doi.org/10.1016/s0009-2509(00)00533-9).
- [79] Reichelt W. Calculation of pressure-drop in spherical and cylindrical packings for single-phase flow. *Chem Ing Tech*. 1972;44. <http://dx.doi.org/10.1002/cite.330441806>. 1068–8.
- [80] Carman PC. *Flow of gases through porous media*. London: Butterworths; 1956.
- [81] Carman PC. Fluid flow through granular beds. *Trans Inst Chem Eng* 1937;15:150–66. [http://dx.doi.org/10.1016/S0263-8762\(97\)80003-2](http://dx.doi.org/10.1016/S0263-8762(97)80003-2).
- [82] Bear J. *Dynamics of fluids in porous media*. New York: Dover Publications, Inc.; 1972. ISBN 0486656756.
- [83] Maier RS, Kroll DM, Bernard RS, Howington SE, Peters JF, Davis HT. Enhanced dispersion in cylindrical packed beds. *Philos Trans Royal Soc London Series a-Math Phys Eng Sci* 2002;360:497–506. <http://dx.doi.org/10.1098/rsta.2001.0951>.